Supplemental Materials

Mirror-symmetry engineering of altermagnetism based on monolayer hexagonal lattices

Han-Bing Li[1, 2] and Zhi-Gang Shao[1, 2, *]

[1] *Guangdong Basic Research Center of Excellence for Structure and Fundamental Interactions of Matter, Guangdong Provincial Key Laboratory of Quantum Engineering and Quantum Materials, School of Physics, South China Normal University, Guangzhou 510006, China*

[2] *Guangdong-Hong Kong Joint Laboratory of Quantum Matter, Frontier Research Institute for Physics, South China Normal University, Guangzhou 510006, China*

(Dated: October 30, 2026)

Note S1. Computational Details

First-principles calculations based on density functional theory (DFT) were performed using the Vienna *ab initio* simulation package [1–3]. The electron–ion interactions were treated with the projector augmented-wave method [4], and a plane-wave cutoff energy of 500 eV was employed. The exchange–correlation energy was described using the Perdew–Burke–Ernzerhof functional within the generalized gradient approximation [5]. Van der Waals interactions were corrected using the DFT-D3 method [6]. To eliminate spurious interactions between periodic images, a vacuum layer of 15 Å was added along the out-of-plane direction. All structures were fully relaxed, with convergence criteria of 1×10^{-5} eV for total energy and 0.01 eV/Å for atomic forces. A $6 \times 6 \times 1$ Monkhorst–Pack k-point mesh [7] was used for structural optimization, while a denser $11 \times 11 \times 1$ mesh was adopted for the calculations of density of states (DOS) and magnetic moments. *Ab initio* molecular dynamics (AIMD) simulations were performed using a $2 \times 2 \times 1$ supercell in the NVT ensemble, employing a Nosé–Hoover thermostat at 300 K. The simulations were run for a total duration of 5 ps with a time step of 2 fs to assess the structural stability at room temperature. Phonon spectra were calculated using density-functional perturbation theory as implemented in the PHONOPY package [8] to further confirm the dynamical stability.

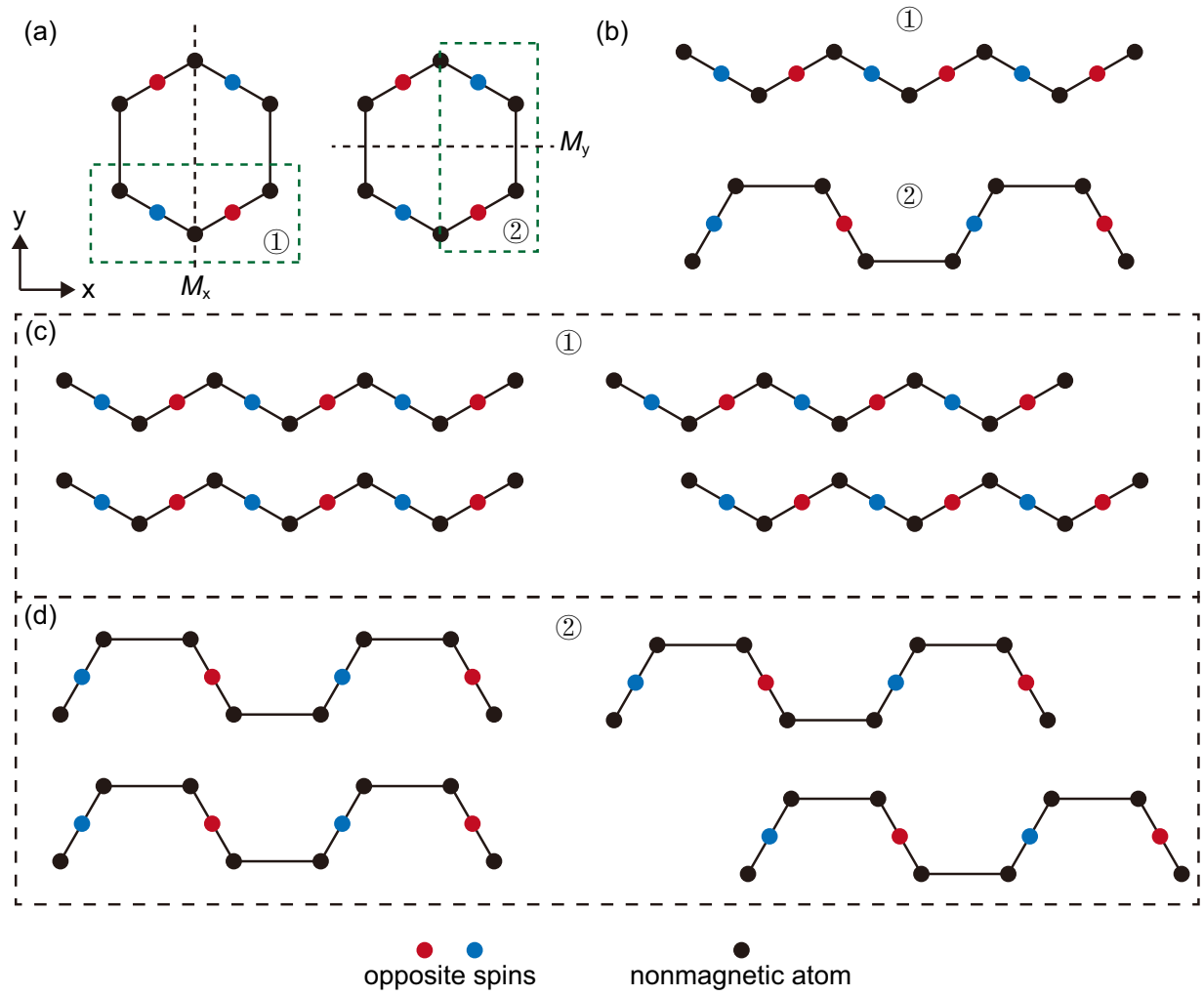


FIG. S1. Design of Q1D altermagnetic models via self-assembly of 1D magnetic chains. (a) Two possible ways of decomposing the 2D hexagonal lattice model along the green dashed boxes. (b) Isolated 1D atomic chain models ① and ②, in which the two opposite-spin sites are related by the mirror operation M_x. (c) and (d) Schematic Q1D models formed by the parallel assembly of chains ① and ② through vertical translation or horizontal sliding. The two antiparallel spin sublattices are related by the $[C_2\|M_x]$ combined operation, satisfying the symmetry requirements of altermagnetism.

Note S2. Verification of the Altermagnetic State in Covalent Organic Framework COF-1

To examine the transferability of the mirror-symmetry-based design principle beyond HGY, we performed structural and magnetic analyses using the covalent organic framework COF-1 as a representative system. As shown in Fig. S2(a), two H atoms used for electronic saturation were removed from both sides of the mirror-symmetry axis of COF-1, thereby breaking the local coordination saturation. Upon removing the H atoms, the unsaturated p orbitals of C1 and C2 give rise to opposite projected magnetic moments of +0.473 and -0.473 μ_B, respectively, and the two atoms are located at mirror-symmetric positions. The total magnetic moment is 0 μ_B per unit cell, confirming the compensated antiparallel spin configuration.

Energy comparison shows that the AFM configuration is lower in energy than the FM configuration by about 1 meV, indicating that the system prefers an antiparallel spin arrangement. The spin-polarized band structure [Fig. S2(b)] exhibits a clear spin splitting along the K_1–K–K_2 path, demonstrating the breaking of PT symmetry. The spin-density distribution [Fig. S2(c)] further confirms that the magnetism mainly originates from the two carbon atoms C1 and C2, which lie on opposite sides of the mirror-symmetry axis and host antiparallel spins. These two antiparallel spin sublattices can be mapped onto each other through the mirror reflection M_x, forming a typical altermagnetic configuration.

This finding provides an additional example of the proposed mirror-symmetry-based design principle and supports its applicability beyond HGY.

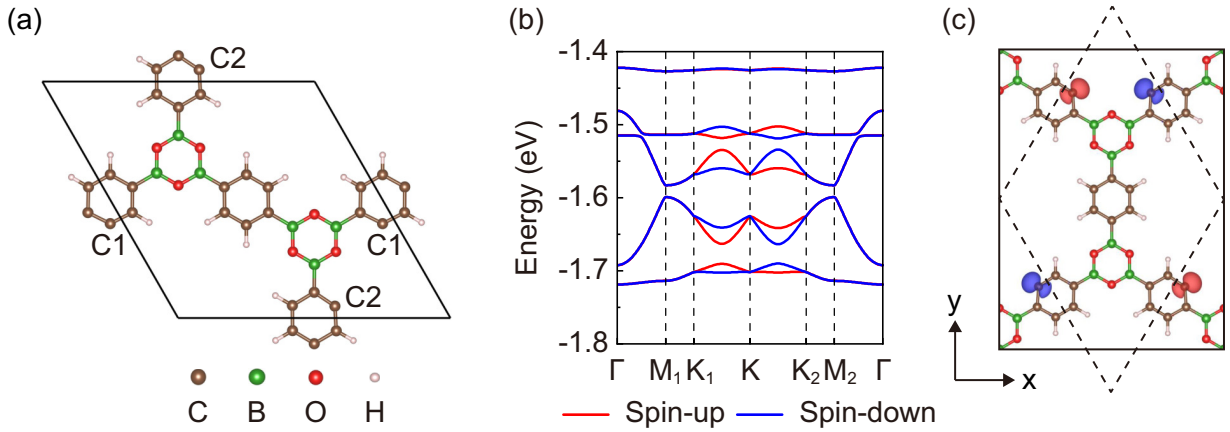


FIG. S2. (a) Geometric structure, (b) non-relativistic spin-polarized band structure, and (c) spin-density distribution of COF-1 after removing two H atoms on both sides of the mirror-symmetry axis. Red and blue denote spin-up and spin-down densities, respectively. The dashed box marks the unit cell of the defective COF-1.

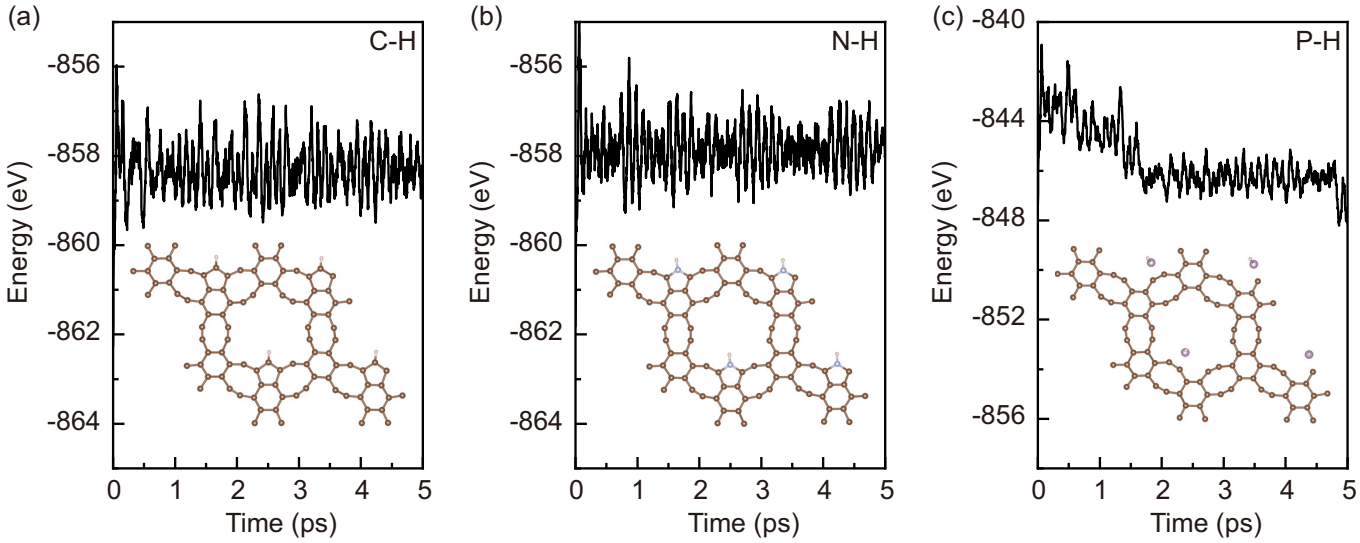


FIG. S3. AIMD energy evolutions and final structural snapshots of the (a) C–H, (b) N–H, and (c) P–H systems at 300 K. After 5 ps, the C–H and N–H structures remain intact, with their total energies fluctuating slightly around constant values, indicating good thermal stability. In contrast, the P–H system exhibits pronounced energy fluctuations accompanied by bond breaking, indicating poor thermal stability.

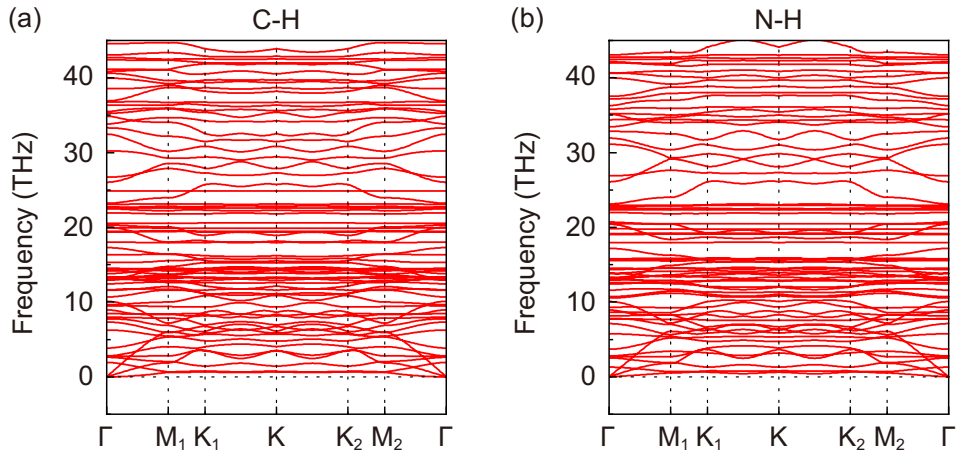


FIG. S4. Phonon spectra of the (a) C–H and (b) N–H systems. No apparent imaginary frequencies are observed along the sampled high-symmetry path, confirming the dynamical stability of both systems.

Note S3. Magnetic Ground States of the C–H and N–H Systems and Néel Temperature of the N–H System

The magnetic exchange interactions and magnetic transition temperature were investigated using the following effective anisotropic Heisenberg Hamiltonian

$$H = -J_1 \sum_{\langle i,j\rangle_1} \mathbf{S}_i \cdot \mathbf{S}_j - J_2 \sum_{\langle i,j\rangle_2} \mathbf{S}_i \cdot \mathbf{S}_j - J_3 \sum_{\langle i,j\rangle_3} \mathbf{S}_i \cdot \mathbf{S}_j + \sum_i \left[D_x (S_i^x)^2 + D_y (S_i^y)^2 + D_z (S_i^z)^2 \right], \tag{1}$$

where J_1, J_2, and J_3 denote the nearest-neighbor, next-nearest-neighbor, and third-nearest-neighbor exchange parameters, respectively. $\mathbf{S}_i$ is the spin vector at magnetic site i, and normalized spin vectors with $|\mathbf{S}_i| = S = 1$ were employed in the Monte Carlo simulations. The parameters D_x, D_y, and D_z denote the effective magnetic anisotropy coefficients along the three Cartesian directions. The exchange parameters were determined by mapping the DFT total energies of four collinear magnetic configurations (AFM-1, AFM-2, AFM-3, and FM), calculated using a $2\times2\times1$ supercell, onto the isotropic exchange part of Eq. (1). Their spin arrangements are illustrated using the N–H system as a representative structure in Fig. S5, and the same arrangements were applied to the C–H system. The corresponding total energies are expressed as

$$E_{\text{AFM-1}} = 4J_1S^2 + 4J_2S^2 + 8J_3S^2 + E_0, \tag{2}$$

$$E_{\text{AFM-2}} = 4J_1S^2 - 4J_2S^2 + E_0, \tag{3}$$

$$E_{\text{AFM-3}} = 4J_1S^2 + 4J_2S^2 - 8J_3S^2 + E_0, \tag{4}$$

$$E_{\text{FM}} = -4J_1S^2 - 4J_2S^2 - 8J_3S^2 + E_0, \tag{5}$$

where E_0 is the energy without magnetic coupling. The exchange parameters are consequently obtained as

$$J_1 = \frac{E_{\text{AFM-3}} - E_{\text{AFM-1}} - 2E_{\text{FM}} + 2E_{\text{AFM-2}}}{16S^2}, \tag{6}$$

$$J_2 = \frac{E_{\text{AFM-1}} - 2E_{\text{AFM-2}} + E_{\text{AFM-3}}}{16S^2}, \tag{7}$$

$$J_3 = \frac{E_{\text{AFM-1}} - E_{\text{AFM-3}}}{16S^2}. \tag{8}$$

Using $S = 1$, we first evaluated the magnetic interactions in the C–H system. Among the four configurations, AFM-2 has the lowest total energy, whereas the altermagnetic configuration corresponds to AFM-1. The calculated exchange parameters are $J_1 = -15.7$ meV, $J_2 = 1.2$ meV, and $J_3 = -0.3$ meV. The positive J_2 indicates FM second-nearest-neighbor coupling, which prevents AFM-1 from becoming the magnetic ground state.

In contrast, AFM-1 is the lowest-energy configuration of the N–H system. Its exchange parameters are $J_1 = -21.4$ meV, $J_2 = -6.4$ meV, and $J_3 = -1.3$ meV. The negative values indicate AFM exchange interactions, which stabilize AFM-1 as the intrinsic altermagnetic ground state. Therefore, the magnetic anisotropy and finite-temperature magnetic behavior were further investigated only for the N–H system. The magnetocrystalline anisotropy energies were evaluated by including spin–orbit coupling (SOC) and comparing the total energies for spin orientations along the x, y, and z directions. For the N–H system, $E_y - E_x = 41.1$ μeV and $E_z - E_x = 31.3$ μeV per unit cell. The x direction therefore has the lowest SOC total energy and is identified as the easy axis. With two effective magnetic sites per unit cell and $S = 1$, taking $D_x = 0$ as the energy reference gives $D_y = 20.6$ μeV and $D_z = 15.7$ μeV per magnetic site.

The Néel temperature was investigated using classical Monte Carlo simulations based on the Metropolis algorithm, as implemented in the MCSOLVER package [9]. A $40 \times 40 \times 1$ spin lattice was employed, with 2×10^5 thermalization sweeps followed by 2×10^6 measurement sweeps at each temperature. To provide a direct comparison with the

previously reported calculations for N-, B-, and S-adsorbed HGY without H functionalization, we first performed simulations in the ideal Ising limit. In this limit, the vector spins in the exchange part of Eq. (1) are replaced by Ising variables $\sigma_i = \pm 1$, while the same J_1, J_2, and J_3 parameters are retained. As shown in Fig. S6, the temperature-dependent specific heat of the N–H system exhibits a peak at approximately 250 K. This Ising-limit peak temperature is higher than the previously reported Ising-model values of 142.7 K for N-adsorbed HGY and 80–210 K for B- and S-adsorbed HGY [10], reflecting the enhanced antiferromagnetic exchange interactions following H functionalization.

However, the Ising model generally overestimates the ordering temperature of a weakly anisotropic 2D magnetic system. We subsequently performed simulations using the anisotropic Heisenberg Hamiltonian in Eq. (1). As shown in Fig. 3(a) of the main text, the specific-heat anomaly occurs at approximately 29 K, giving an estimated Néel temperature of 29 K.

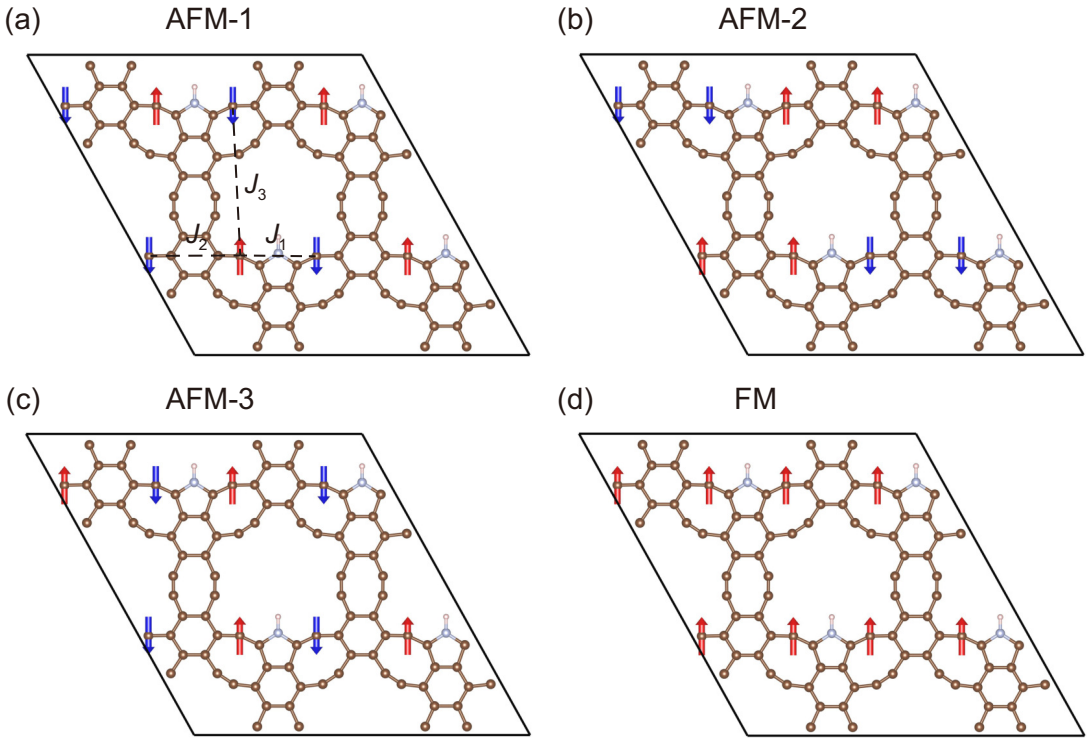


FIG. S5. Collinear magnetic configurations illustrated using the N–H system as a representative structure. Red and blue arrows represent spin-up and spin-down, respectively. J_1, J_2, and J_3 represent the nearest-neighbor, next-nearest-neighbor, and third-nearest-neighbor exchange interactions, respectively.

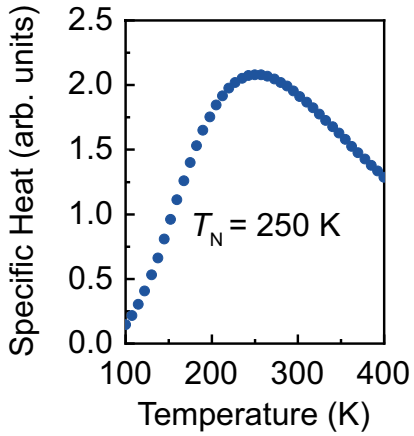


FIG. S6. Temperature-dependent specific heat of the N–H system obtained in the ideal Ising limit. The specific-heat peak at approximately 250 K provides an upper-bound temperature scale for comparison of the exchange strength.

Note S4. Stacking-Dependent Magnetism in N–H-Embedded HGY Bilayers

To examine whether the monolayer altermagnetic state can persist in a bilayer, we constructed three representative stacking arrangements from two identical N–H-embedded HGY monolayers: AA, R180, and S1/2 [Fig. S7(a)–(c)]. In AA stacking, the two layers are directly aligned without any relative in-plane rotation or translation. R180 was generated by rotating the upper layer by 180° about the out-of-plane axis through the in-plane origin, whereas S1/2 was obtained by translating the upper layer by $\mathbf{a}/2$ without rotation. All bilayer structures were relaxed. The relaxed average interlayer distances are 3.645, 3.621, and 3.420 Å for AA, R180, and S1/2, respectively.

For each stacking, the intralayer altermagnetic spin pattern was retained, and two interlayer spin arrangements were considered. Here, interlayer AFM and FM refer to antiparallel and parallel alignment, respectively, of the nearest magnetic carbon sites in adjacent layers, as illustrated in Fig. S7. The relative energies are summarized in Table S1. The interlayer AFM configuration is lower in energy than the FM configuration by 43.4, 15.3, and 19.0 meV per bilayer unit cell for AA, R180, and S1/2, respectively. Among the six configurations examined, S1/2-AFM has the lowest energy. AA-AFM and R180-AFM lie higher by 82.0 and 34.1 meV per bilayer unit cell, respectively.

TABLE S1. Relative energies of the interlayer AFM and FM configurations for three representative N–H-embedded HGY bilayer stackings. Energies are given in meV per bilayer unit cell, with S1/2-AFM taken as the reference. Positive $\Delta E = E_{\mathrm{FM}} - E_{\mathrm{AFM}}$ indicates that the interlayer AFM arrangement is energetically preferred.

Stacking	E_{AFM}	E_{FM}	ΔE
AA	82.0	125.4	43.4
R180	34.1	49.4	15.3
S1/2	0.0	19.0	19.0

The non-SOC spin-resolved band structures of the lower-energy AFM configurations show a clear stacking dependence. For AA and R180, no resolvable spin splitting is observed along the plotted path. In contrast, S1/2-AFM exhibits alternating momentum-dependent spin splitting. Its total magnetic moment is zero, and the principal magnetic carbon sites carry opposite local moments of approximately $\pm 0.514\,\mu_{\mathrm{B}}$ within each layer, while the N and H moments are negligible.

Structural analysis shows that the relaxed S1/2 structure retains the vertical mirror M_x. This mirror exchanges the opposite-spin carbon sites within each layer, giving the spin-group operation $[C_2 \parallel M_x]$, where C_2 denotes a 180° spin-space rotation that reverses the collinear spin direction. In the S1/2-AFM configuration, corresponding sites in the two layers have parallel spins, whereas the nearest interlayer magnetic sites have antiparallel spins. Thus, the interlayer glide reflection $\{M_z \mid \mathbf{a}/2\}$, even if retained, would connect same-spin sites and would not enforce spin degeneracy. The compensated magnetization, mirror-related opposite-spin sublattices, and alternating nonrelativistic spin splitting together support the altermagnetic character of this bilayer configuration.

These results demonstrate that altermagnetic characteristics can persist beyond the monolayer in an appropriately stacked bilayer. The stacking-dependent band structures highlight the importance of stacking geometry and interlayer magnetic alignment when extending the monolayer system to multilayers.

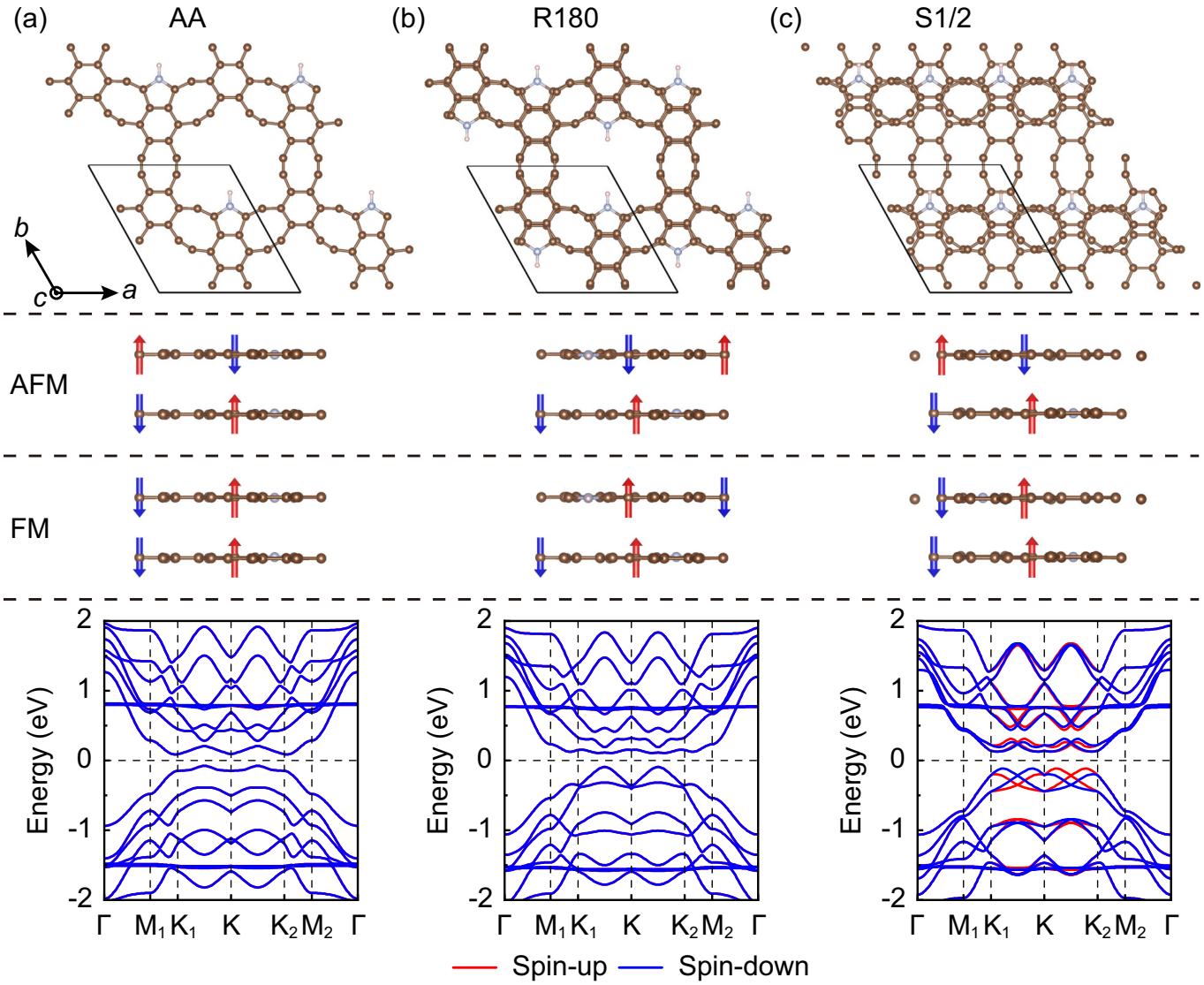


FIG. S7. Structures, interlayer spin arrangements, and non-SOC spin-resolved band structures of N–H-embedded HGY bilayers with (a) AA, (b) R180, and (c) S1/2 stacking. The top row shows the top views, with black outlines indicating the unit cells. The lattice directions a, b, and c are indicated in the top row. The middle rows illustrate the interlayer AFM and FM configurations, defined by the relative spin alignment of the nearest magnetic carbon sites in adjacent layers. Red and blue arrows denote opposite local spin directions. The bottom row shows the band structure of the lower-energy AFM configuration for each stacking. Red and blue curves represent spin-up and spin-down states, respectively. The energy zero is set to the Fermi level.

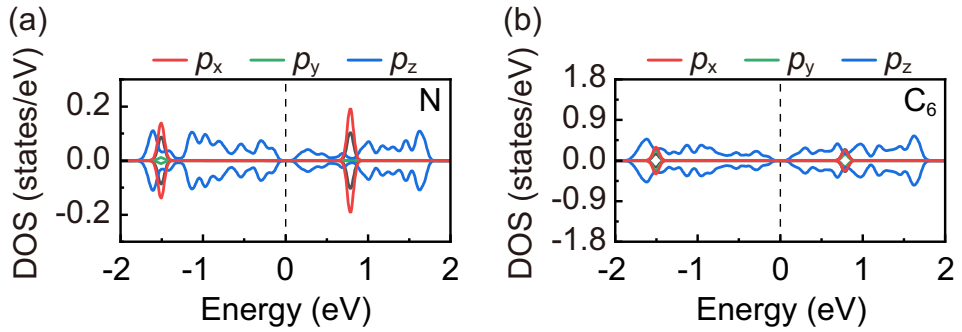


FIG. S8. Orbital-resolved DOS of the (a) N atom and (b) carbon ring C_6.

Note S5. Global Orbital Centers and Electron Occupation

In Fig. S9, the global orbital centers (ε_g) of C1, C2, N, and C_6 are calculated over the full energy range, defined as

$$\varepsilon_g = \frac{\int_{-\infty}^{+\infty} E\, g(E)\, dE}{\int_{-\infty}^{+\infty} g(E)\, dE}, \tag{9}$$

where $g(E)$ represents the DOS. The global orbital center characterizes the overall energy distribution of the projected DOS. Its spin-dependent shift can help interpret differences in orbital occupation, whereas the occupation numbers (N) for each spin channel (as labeled in Fig. S9) are evaluated separately by integrating the projected DOS up to the Fermi level (E_F),

$$N = \int_{-\infty}^{E_F} g(E)\, dE. \tag{10}$$

It should be noted that integrating the projected DOS accounts only for the electron density captured within the atom-centered projection regions, while part of the electron density may lie outside these regions due to orbital hybridization. Consequently, the resulting projected occupation numbers can appear relatively small. Therefore, the values in Fig. S9 are used to compare the spin-up and spin-down occupations and evaluate their spin compensation.

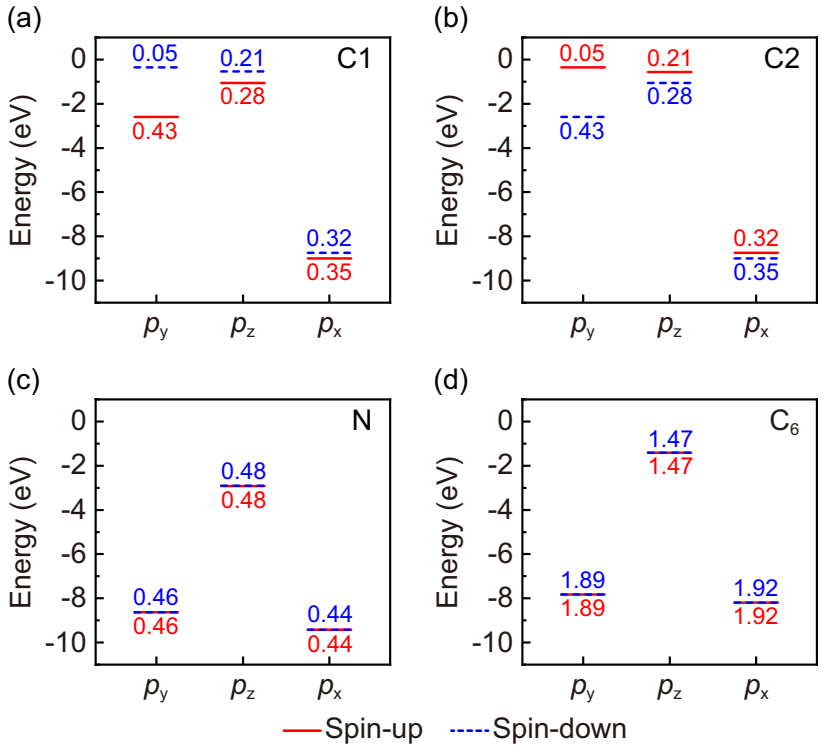


FIG. S9. Orbital energy levels (global orbital centers) of (a) C1, (b) C2, (c) N, and (d) C_6. The numbers indicate the electron occupation of each orbital.

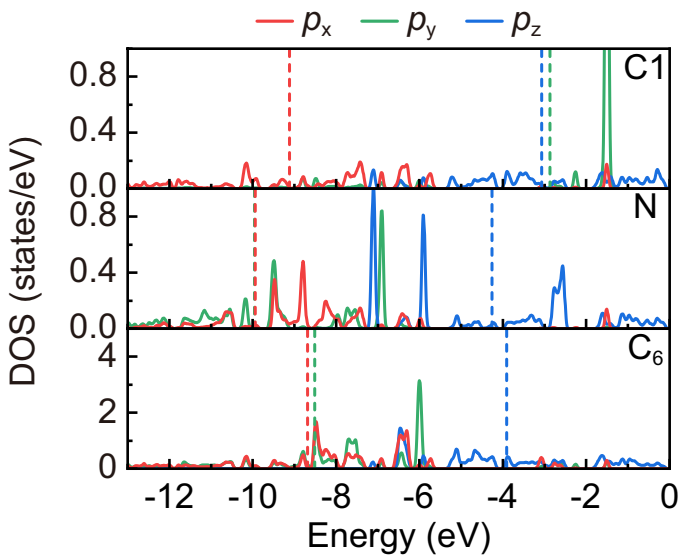


FIG. S10. Orbital-resolved DOS and occupied-state orbital energy levels (dashed lines) of C1, N, and C_6.

Note S6. Altermagnetic State in N–F Embedded HGY Monolayer

The magnetic properties of the N–F system were investigated following the same procedure as that used for the N–H system. Among the four collinear magnetic configurations considered, AFM-1 has the lowest total energy and corresponds to the altermagnetic ground state. The calculated exchange parameters are $J_1 = -18.4$ meV, $J_2 = -5.9$ meV, and $J_3 = -1.2$ meV, indicating antiferromagnetic exchange interactions. The SOC total energies satisfy $E_x \approx E_z < E_y$, indicating an effective xz easy plane. Taking $D_x = D_z = 0$, the anisotropy coefficient is $D_y = 0.74$ μeV per magnetic site. Subsequently, Monte Carlo simulations were performed using the anisotropic Heisenberg model. As shown in Fig. S11(b), the specific heat exhibits an anomaly at approximately 26 K, which is slightly lower than the corresponding temperature for the N–H system.

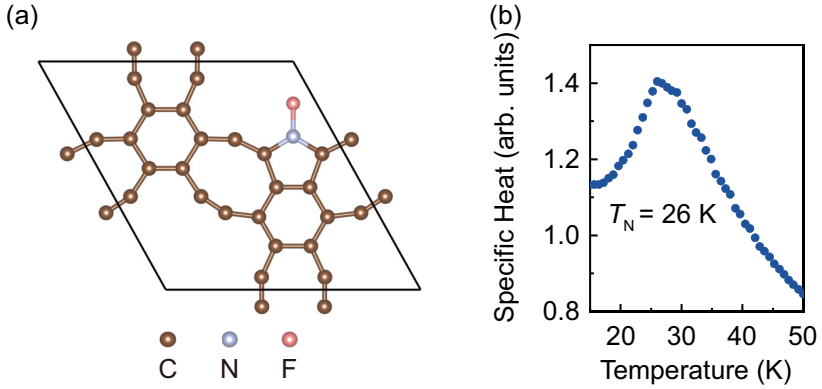


FIG. S11. (a) Geometric structure of the N–F-embedded HGY monolayer and (b) temperature-dependent specific heat obtained from the anisotropic Heisenberg model.

Non-relativistic band structure calculations further confirm the altermagnetic behavior. As shown in Fig. S12(a), a pronounced spin splitting is observed along the K_1–K–K_2 path, with a maximum splitting near the Fermi level reaching 135 meV, clearly demonstrating the altermagnetic characteristics of the N–F system. The spin-density distribution shown in Fig. S12(b) reveals that the magnetic moments mainly originate from the C1 and C2 atoms, which possess opposite spins. Meanwhile, C1 and C2 remain related by the M_x symmetry operation rather than spatial inversion, resulting in the breaking of PT symmetry and consequently giving rise to the altermagnetic state.

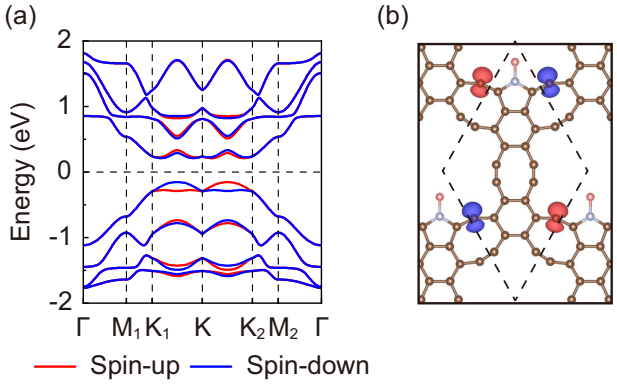


FIG. S12. (a) Non-relativistic spin-polarized band structure and (b) spin-density distribution of the N–F system. Red and blue denote spin-up and spin-down densities, respectively. The dashed box indicates the unit cell.

Note S7. Optimized Structures of the N–H and N–F Systems

Structure S1. N–H-embedded HGY

```
N-H-HGY
1.00000000000000
10.5840347035420628     0.0000000000000000     0.0000000000000000
-5.2920105828664852     9.4672672551536152     0.0000000000000000
0.0000000000000000     0.0000000000000000    15.0000000000000000
C    N    H
24     1     1
Direct
0.9104237228322716  0.5981975466312232  0.5036346235762220
0.0665405118794093  0.4095585258601865  0.5043019632226450
0.4033591279899299  0.3380949664628589  0.5024803234304568
0.6015266553431330  0.6593963546922609  0.5040670131070053
0.6525140263569810  0.0565802473157284  0.5001431491710091
0.3404362253537265  0.9269038229879036  0.5013352284537989
0.5864657113248647  0.9269058091372983  0.5013348751134968
0.4040693597989036  0.0565788824600139  0.5001525501720980
0.3430121654319240  0.4095513186576251  0.5043146540339459
0.6877727557514604  0.5981991837602766  0.5036345547331361
0.0578671222666719  0.6593977499352590  0.5040621300542694
0.9347421685206695  0.3380962540748557  0.5024541358896530
0.7949661118790480  0.3208456892243307  0.5008292457661917
0.1919136981866317  0.6623298902202776  0.5040426593671190
0.6599658668977312  0.4513584531420469  0.5015110229260601
0.3320780612916441  0.5327417844164327  0.5048769273239700
0.5273761126083116  0.1926913387124133  0.4997743650799422
0.4638455432475385  0.7903266524344364  0.5027674106818073
0.3264823568296553  0.7903287513873435  0.5027672297289818
0.6653172525002022  0.1926942337709235  0.4997639802791790
0.4704153888948165  0.6623306556156888  0.5040458340635483
0.5258738085967741  0.3208403311980746  0.5008456485661515
0.2006640692934410  0.5327454820192050  0.5048764293513841
0.7913940132278424  0.4513624548717650  0.5015053817149591
0.8390836499210440  0.6781693901686402  0.5050846977485655
0.8926868401724580  0.7853716855679604  0.5062889945574480
```

Structure S2. N–F-embedded HGY

```
N-F-HGY
1.00000000000000
10.5893755074828491     0.0000000000000000     0.0000000000000000
-5.2942968670132640     9.4715321860749011     0.0000000000000000
0.0000000000000000     0.0000000000000000    15.0000000000000000
C    N    F
24     1     1
Direct
0.9109516601747309  0.5953841251548549  0.5073806412615032
0.0658634002486612  0.4085610121893473  0.5053953064367720
0.4026867245878000  0.3368359246416177  0.5033053992859454
0.6004296399462216  0.6580471363917196  0.5058808110290578
0.6518497186523685  0.0552047194387897  0.4990045986848105
0.3398959386412423  0.9256604190141610  0.4998517224210266
0.5857505583479399  0.9256419285521684  0.4998311733272700
0.4033741080007329  0.0552212818658567  0.4990253764344333
0.3426963221420012  0.4085470422650706  0.5053914034922424
0.6844315691380636  0.5953849658980899  0.5073831774712063
0.0576026639362664  0.6580570027266430  0.5058881658132598
0.9341609345508248  0.3368424178035561  0.5032866639072948
0.7942723001702741  0.3191794714188318  0.5013143622763166
0.1918359018434001  0.6612588551887416  0.5043019366935938
0.6589642375717942  0.4493194822525088  0.5023767522919940
0.3314802337888843  0.5315779813899244  0.5057526620624605
0.5267013639826655  0.1911833148849394  0.4993217914742270
0.4632788446499061  0.7891569102185358  0.5016059402019134
0.3258689977700624  0.7891680527949361  0.5016146775137432
0.6644971165110121  0.1911836315180326  0.4993132570849137
0.4694149509491084  0.6612586462681836  0.5042896692640959
0.5249283411296480  0.3191866231133330  0.5013299560270157
0.2000950357327915  0.5315786912815684  0.5057573227851623
0.7903631672756961  0.4493178278302549  0.5023699847311067
0.8356688505981580  0.6713488763763443  0.5171295993919689
0.9079613038663740  0.8159423051929039  0.5054719586744190
```

* zgshao@scnu.edu.cn

[1] G. Kresse and J. Furthmüller, Efficient iterative schemes for ab initio total-energy calculations using a plane-wave basis set, Phys. Rev. B **54**, 11169 (1996).

[2] G. Kresse and J. Furthmüller, Efficiency of ab-initio total energy calculations for metals and semiconductors using a plane-wave basis set, Comp. Mater. Sci. **6**, 15 (1996).

[3] G. Kresse and D. Joubert, From ultrasoft pseudopotentials to the projector augmented-wave method, Phys. Rev. B **59**, 1758 (1999).

[4] P. E. Blöchl, Projector augmented-wave method, Phys. Rev. B **50**, 17953 (1994).

[5] J. P. Perdew, K. Burke, and M. Ernzerhof, Generalized Gradient Approximation Made Simple, Phys. Rev. Lett. **77**, 3865 (1996).

[6] S. Grimme, J. Antony, S. Ehrlich, and H. Krieg, A consistent and accurate ab initio parametrization of density functional dispersion correction (DFT-D) for the 94 elements H-Pu, J. Chem. Phys. **132**, 154104 (2010).

[7] H. J. Monkhorst and J. D. Pack, Special points for Brillouin-zone integrations, Phys. Rev. B **13**, 5188 (1976).

[8] A. Togo and I. Tanaka, First principles phonon calculations in materials science, Scripta Mater. **108**, 1 (2015).

[9] L. Liu, X. Ren, J. Xie, B. Cheng, W. Liu, T. An, H. Qin, and J. Hu, Magnetic switches via electric field in BN nanoribbons, Appl. Surf. Sci. **480**, 300 (2019).

[10] H.-B. Li and Z.-G. Shao, Achieving altermagnetism in monolayer holey graphyne via atomic manipulation, Phys. Rev. B **111**, 214420 (2025).